J. Fluid Mech. (2007), *vol.* 583, *pp.* 443–458.
doi:10.1017/S0022112007006416 Printed in the United Kingdom

Structure of a stratified tilted vortex

NICOLAS BOULANGER, PATRICE MEUNIER AND STÉPHANE LE DIZÈS

Institut de Recherche sur les Phénomènes Hors Équilibre, CNRS/Universités Aix-Marseille I&II, 49, rue F. Joliot-Curie, B.P. 146, F-13384 Marseille cedex 13, France

(Received 13 July 2006 and in revised form 8 March 2007)

The structure of a columnar vortex in a stably stratified fluid is studied experimentally and theoretically when the vortex axis is slightly tilted with respect to the direction of stratification. When the Froude number of the vortex is larger than 1, we show that tilting induces strong density variations and an intense axial flow in a rim around the vortex. We demonstrate that these characteristics can be associated with a critical-point singularity of the correction of azimuthal wavenumber $m = 1$ generated by tilting where the angular velocity of the vortex equals the Brunt–Väisälä frequency of the stratified fluid. The theoretical structure obtained by smoothing this singularity using viscous effects (in a viscous critical-layer analysis) is compared to particle image velocimetry measurements of the axial velocity field and visualizations of the density field and a good agreement is demonstrated.

1. Introduction

Small intense vortices, characterized by large Froude and Rossby numbers, are present in both the atmosphere and the ocean. The goal of the present paper is to determine their structure when the vortex axis is slightly tilted with respect to the direction of stratification.

In the atmosphere, the dynamics is often governed by large-scale motion induced by the baroclinic instability of thermal fronts. However, secondary instabilities have also been evidenced (Neiman, Shapiro & Fedor 1993) and they may lead to the formation of small intense cyclones (Polavarapu & Peltier 1993; Garnier, Métais & Lesieur 1996). These vortices are often too small to be described by meteorological models, but they can be very damaging during strong storms (Lesieur, Métais & Garnier 2000). Understanding the dynamics of these structures constitutes one of the motivations of this work. The most intense of these structures are columnar vortices with large Froude numbers (their maximum angular velocity is larger than the Brunt–Väisälä frequency of the fluid). We think that the analysis performed in this paper could provide some information on their dynamics, when their axis is tilted with respect to the direction of stratification.

Vortices are also observed in the ocean. For instance, they can form close to islands or near headlands by a barotropic instability of the flow generated by the tide. The resulting vortices are generally strongly tilted owing to the weak slope of coastal regions (Pawlak *et al.* 2003) and it has been argued that this could be the cause of intense vertical mixing (Farmer, Pawlowicz & Jiang 2002). Here, we shall see that, if the vortices are sufficiently intense, tilt angle need not be important in inducing strong vertical displacements.

The effect of a stable stratification on the dynamics and stability of vortices has been the subject of numerous works. The inviscid criteria for two-dimensional shear instability and centrifugal instability are not affected by stratification (see for instance Hopfinger & van Heijst 1993). However, other instabilities usually active when several vortices interact are modified: the elliptic instability is stabilized (Kerswell 2002) and the Crow instability is replaced by a new zigzag instability (Billant & Chomaz 2000) when the stratification is sufficiently strong. For a single vortex with a large Froude number, Cariteau & Flór (2003) also reported a new instability characterized by a rim region of strong vertical mixing, but they did not propose any instability mechanism (see Cariteau 2005). We shall argue below that this instability was probably due to a misalignment of the vortex axis with the direction of stratification.

As far as we know, the effects of vortex tilting have not been studied in the laboratory. When the vortex axis is tilted with respect to the direction of stratification, the azimuthal symmetry of the vortex is broken and non-axisymmetric corrections of azimuthal wavenumber $m = 1$ are created. For large Reynolds numbers and Froude numbers greater than 1, we shall see that these corrections are characterized by strong density variations and intense axial flow near a particular radial location. We shall associate this location with the critical-point singularity where the angular velocity of the vortex is equal to the Brunt–Väisälä frequency of the fluid. These singularities, which appear in the inviscid description of linear perturbations, are known to play an important role in shear instabilities (Drazin & Reid 1981; Maslowe 1986), and internal wave propagation (e.g. Booker & Bretherton 1967). They have also been shown to be present in the analysis of the deformation of a vortex by a rotating strain field (Le Dizès 2000). In this case, the critical-point singularity occurs in the $m = 2$ azimuthal correction at the location where the angular velocity of the vortex is equal to the angular frequency of the strain. Le Dizès (2000) showed that the singularity can be smoothed by introducing either viscous or nonlinear effects in the critical-layer region as for planar shear flows.

The theoretical description of the correction induced by tilting will be obtained by a similar method. We shall demonstrate that the characteristics obtained by smoothing the critical-point singularity with viscous effects allows the reproduction of the experimental observations and measurements.

The paper will be organized as follows. In § 2, the experimental set-up is presented and the characteristics of the vortices when the axis is not tilted are discussed. In § 3, experimental evidence for the critical-layer region is given and the theoretical framework is introduced. In § 4, the viscous critical-layer analysis is performed and the theoretical predictions for axial flow velocities are compared to particle image velocimetry (PIV) measurements. In the last section, the main results of the paper are briefly summarized. We also introduce the instability which develops in the critical-layer region and which is the subject of a companion paper (Boulanger, Meunier & Le Dizès 2007).

2. Experimental set-up and base flow

2.1. *Experimental details*

The experimental set-up is represented schematically in figure 1. The experiments are performed in a 1.50 m long, 0.75 m wide and 0.50 m high Plexiglas tank. The tank is filled with linearly stratified fluid up to a height of 0.45 m. The linear stratification is established by the two-tank method, using clear water in the first tank and salt water with a density varying between $1100\,\mathrm{kg\,m^{-3}}$ and $1190\,\mathrm{kg\,m^{-3}}$ in the second tank. The

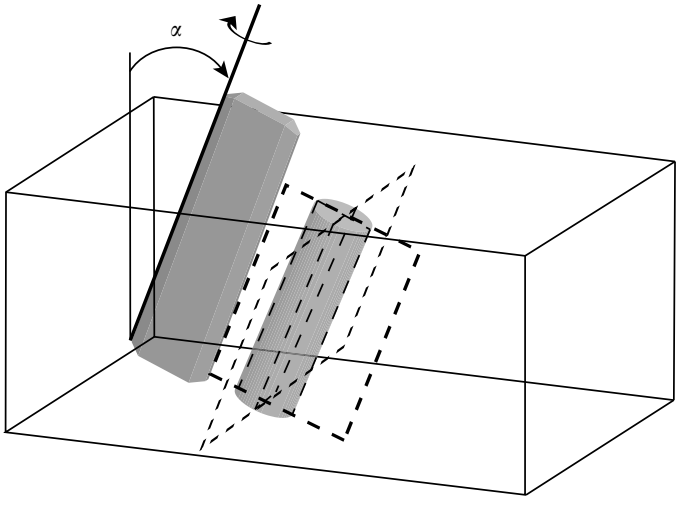

FIGURE 1. Experimental set-up. The rotation of the grey plate around its upper edge generates a vortex inclined at an angle α with respect to the vertical.

density gradient is deduced from density measurements of small samples of fluid every 5 cm, using a densitometer Anton Paar DMA 35N with an accuracy of $0.1\,\mathrm{kg\,m^{-3}}$. By varying the effective depth of fluid between 0.2 m and 0.45 m, we have been able to obtain a Brunt–Väisälä frequency ranging from $1.5\,\mathrm{rad\,s^{-1}}$ to $3\,\mathrm{rad\,s^{-1}}$. For small depth of fluid, a uniform layer of maximal density ($1190\,\mathrm{kg\,m^{-3}}$) and 0.10 m thickness was added under the linearly stratified fluid in order to avoid bottom effects.

The vortex is created by impulsively rotating a flap in the fluid initially at rest. This generates a two-dimensional shear layer detaching at the edge of the flap and rolling-up in a vortex. This method is convenient since it creates a laminar two-dimensional vortex. It has been used frequently for the study of three-dimensional instabilities (Crow, elliptic, zigzag or centrifugal) of vortices (see Leweke & Williamson 1998; Billant & Chomaz 2000; Meunier & Leweke 2005). In our set-up, the flap is made of aluminium and has dimensions $0.1 \times 0.6\,\mathrm{m^2}$, and is sharpened at its free edge, i.e. where the shear layer detaches. It is rotated by a computer-controlled step-motor as in Meunier & Leweke (2005). The motion of the flap has been chosen carefully, through empirical improvements, to create a nearly Gaussian vortex, and to avoid roll-up instabilities (Kelvin–Helmholtz instabilities of the shear layer) and stopping vortices. The motion profile (angular velocity as function of angle in degrees) that was finally adopted is

$$\dot{\Theta} = \dot{\Theta}_{max} \frac{0.42}{\Theta + 0.017} \left[1 + \mathrm{e}^{-(\Theta/0.26)^{5/4}}\right], \tag{2.1}$$

and consists of a rapid acceleration of the flap, followed by a gradual slow-down up to the angle of $\pi/2$ rad. The circulation of the vortex is varied by modifying the maximum angular velocity $\dot{\Theta}_{max}$ between 0.01 and $0.5\,\mathrm{rad\,s^{-1}}$. The inclination of the vortex is obtained by tilting the flap with respect to the vertical in the initial plane of the flap (see figure 1).

Quantitative measurements of velocity fields are obtained by PIV. The flow is seeded with particles of variable density so that they are homogeneously distributed through the whole depth. We have used Sphericel hollow glass spheres 110P8 (Potter Industries), with a density of approximately 1.1, and a diameter ranging from 11 to

18 μm. The particles are illuminated by a luminous sheet of 3–5 mm thickness, created by a continuous 5 W argon-ion lasr. Image pairs are recorded by a digital PIV camera (Kodak Megaplus Es 4.0) with a resolution of 2048×2048 pixels at a rate of 5 fields per second, and treated by a cross-correlation algorithm (Meunier & Leweke 2003).

Measurements have been made in three different planes. The first one is perpendicular to the vortex axis and provides the characteristics of the initial vortex. The other two planes correspond to two orthogonal longitudinal planes, one plane being vertical ($\theta = 0$) and the other being tilted ($\theta = \pi/2$) (figure 1). In the vertical longitudinal plane, the vortex appears tilted in the images, whereas in the tilted longitudinal plane, the vortex appears vertical in the images. The displacement of the flap also induces a weak background velocity field which slowly moves the vortex away from the flap. This slow translating movement is used to scan the complete vortex volume without moving the plane of measurement. It allows the determination of the axial component of the velocity field in the whole three-dimensional space.

Shadowgraph visualizations were also carried out, to observe the two-dimensional and three-dimensional spatial distribution of density inside the vortex. For this purpose, the stratified fluid is illuminated by a large beam of parallel light, created by an intense light placed behind a small diaphragm located 2 m from the tank. Since the refraction index of the fluid depends on its density, the rays are bent toward the larger densities. To first order, the rays are thus deviated toward the floor. To second order, they will be deviated according to the spatial distribution of density inside the vortex. By placing a large lens (of diameter 0.3 m and of focal distance 0.5 m) behind the tank, it is thus possible to obtain an image of the density distribution. These images are recorded by a 2000×2000 pixels grey-scale camera located behind the focal point of the lens. For better visualizations, a small disk of 1 mm diameter has been positioned exactly at the focal point of the lens. This process, called strioscopy, allows us to mask the rays which are not deviated by the density perturbations of the vortex, and enhances the contrast of the images. In strioscopy measurement, it can be shown that the intensity of the images is proportional to the Laplacian of the refraction index, i.e. of the density. However, this property will not be used. In our experiments, we will simply use strioscopy to reveal the qualitative features of the flow.

2.2. *Vortex characteristics*

Figure 2(*a*) shows a typical velocity field obtained by PIV measurements in a horizontal plane, when the vortex axis is exactly vertical. The velocity field is very close to axisymmetric. The spatial resolution is very high (approximatively 20 vectors within the vortex core) such that the uncertainties on the velocity field are small. In figure 2(*a*), the spatial resolution has been reduced by a factor 2 for visualization purposes. The uncertainties on the vorticity field are larger, but still remain lower than 5%. Figure 2(*b*) presents the velocity profiles obtained from an angular averaging of the velocity field shown in figure 2(*a*). The velocity profile is approximated well by the profile of a Gaussian vortex (Lamb–Oseen), whose angular velocity is given by:

$$\Omega_0(r) = \frac{v_\theta(r)}{r} = \frac{\Gamma}{2\pi r^2}\left(1 - \mathrm{e}^{-r^2/a^2}\right). \tag{2.2}$$

In our experiments, the circulation was varied between 17 and 42 $\mathrm{cm}^2\,\mathrm{s}^{-1}$. The core size a is slowly varying with time between 0.9 and 1.1 cm owing to viscous effects, but this dependency can be neglected on the time scale we are considering.

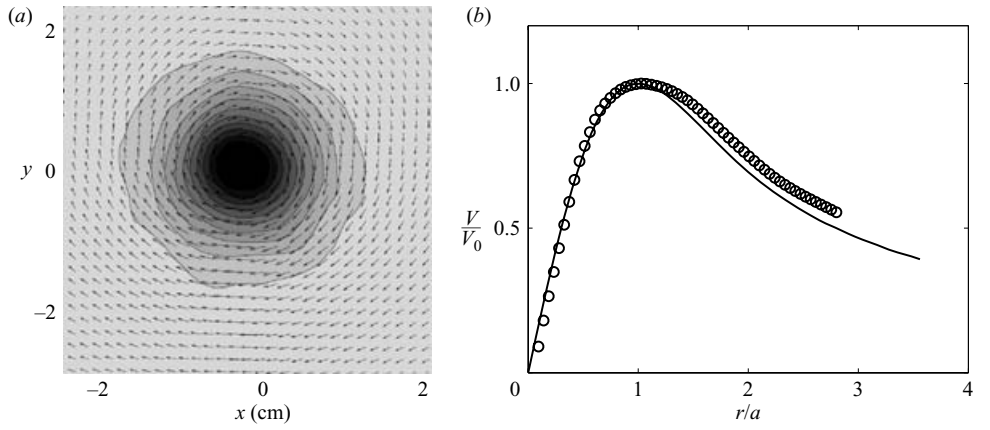

FIGURE 2. Velocity field of the vortex as obtained by PIV measurement in a horizontal cross-section. (*a*) Two-dimensional velocity field and vorticity contours. (*b*) Azimuthal velocity profile measured by PIV and fitted by (2.2) for a Gaussian vortex (solid line). Here, $Re = 370$.

We will non-dimensionalize lengths by the vortex core size a, since it is the only relevant length scale of the flow. Moreover, the inverse of the angular velocity at the centre of the vortex $\Omega_0(r=0) = \Gamma/2\pi a^2$ will be used as the time scale of the flow. This leads to non-dimensionalizing the velocity by $a\Omega_0(0)$. Finally, we will non-dimensionalize densities by the density of the fluid ρ_f at $z=0$.

Our system is characterized by five non-dimensional parameters α, Re, F, Sc and L. The first parameter α is the tilt angle between the vortex and the vertical. It was varied between 0 and 0.26 rad. The Reynolds number Re characterizes the strength of the vortex: it is defined from the circulation of the vortex by $Re = \Gamma/(2\pi\nu)$ (ν being the kinematic viscosity of the fluid) and ranges from 240 to 800. The stratified fluid is characterized by its Brunt–Väisälä frequency $N = \sqrt{-(g/\rho)(\partial\rho/\partial z)}$ from which we define the Froude number $F = \Omega_0(0)/N$. In our experiments, the Froude number ranges from 1.5 to 5. The Schmidt number $Sc = \nu/\kappa$ is the ratio between the viscous diffusivity and the diffusivity of the salt; it is roughly equal to 700 for salted water, which renders the diffusion of salt negligible. The last parameter L compares the vertical stratification length to the vortex core size: $L = \rho/(a\partial\rho/\partial z)$. In our experiments, this parameter ranges between 100 and 400.

3. A critical layer in tilted vortices

3.1. *Experimental evidence*

Figure 3(*a*) shows a side view of the vortex by strioscopic visualizations for an inclination angle $\alpha = 0.12$ rad. This photograph reveals two white strips going from the bottom to the top of the image, with the same angle $\alpha = 0.12$ rad. They are nearly symmetrically located around the vortex axis, which is a barely visible blurry bright line going through the centre of the image. These white strips appear progressively during the vortex formation, and become brighter and brighter as time evolves. After a saturation time of a few seconds they remain stationary during the whole experiment, if the Reynolds number is sufficiently small. These strips reveal a strong density variation (stronger than the radial variations induced by the vortex) concentrated in a

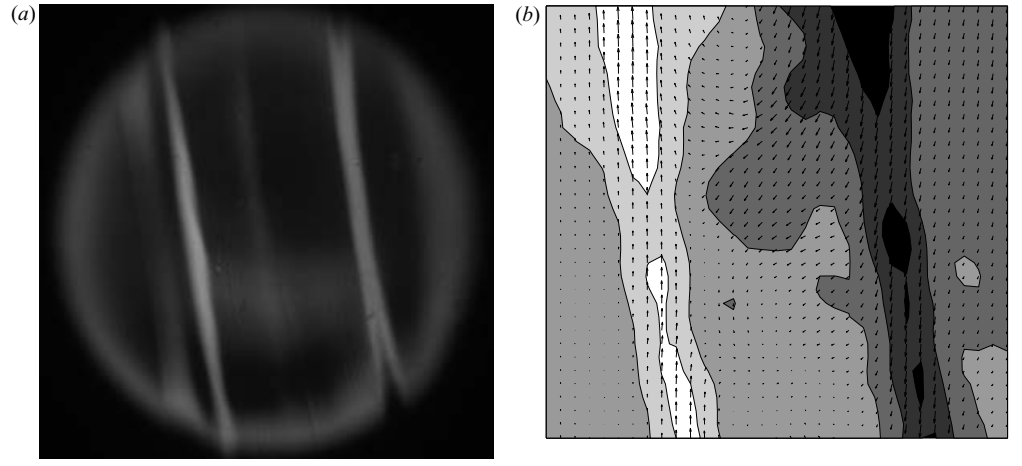

FIGURE 3. View of the vortex approximately five rotation periods after its formation, in a vertical longitudinal plane. (*a*) Density contrast visualized by strioscopy ($Re = 720$, $F = 5$, $\alpha = 0.12$ rad and $r_c = 2.2a$). (*b*) Instantaneous velocity field measured by PIV ($Re = 450$, $F = 3.2$, $\alpha = 0.07$ rad and $r_c = 1.7a$). The grey-scale contours correspond to the vertical velocity component.

thin region at the periphery of the vortex, which we shall see below can be attributed to a critical-layer singularity.

Figure 3(*b*) represents the velocity field superimposed on the axial velocity contours in the same vertical longitudinal plane as in figure 3(*a*), but with a smaller tilt angle $\alpha = 0.07$ rad. For a vertical vortex, the axial velocity is equal to zero. Here, for this small value of the tilt angle, we observe a strong axial velocity field. This axial velocity field is concentrated in two strips located symmetrically with respect to the vortex axis. The velocity is downward on the upper side of the vortex and upward on the lower side. These strips create a pattern similar to the density variation pattern observed in figure 3(*a*).

This strip-like pattern is not observed for a vertical vortex. For large Reynolds numbers, it appears as soon as the inclination angle is above 2°–3°. It is also observed for moderate Froude numbers between 1 and 5, only. It is possible to measure the radial position where these strips are located in both shadowgraph visualizations and PIV velocity fields. This position is indicated by symbols in figure 4 as a function of the inverse of the Froude number $1/F = N/\Omega_0(0)$. The solid curve gives the location of the critical-point singularity r_c at which the angular velocity $\Omega_0(r_c)$ is equal to the Brunt–Väisälä frequency N. As can be observed, the symbols are very close to the curve. This is the first indication that the strips could be associated with a critical-layer phenomenon. We shall see below that this observation will allow the construction of a theoretical model to describe the flow in the neighbourhood of the critical point.

This link between strips and critical points readily explains why strips have been observed only for moderate Froude numbers above 1. When the Froude number is smaller than unity, there is no critical-point singularity, so no strip is expected to appear. When the Froude number is increased above unity, the critical point moves away from the vortex centre and the strength of the singularity decreases. Density variations and axial flow generation are thus expected to become weaker and to move progressively outside the observation domain.

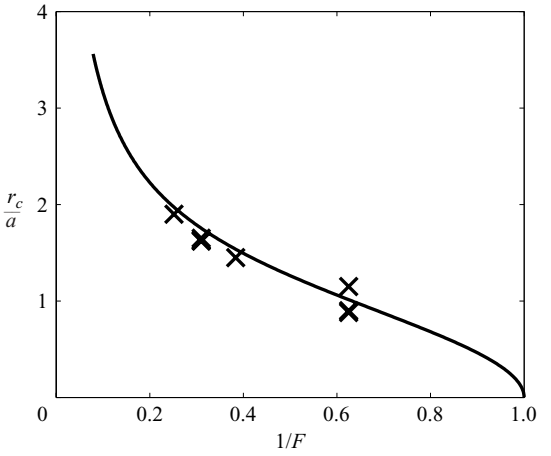

FIGURE 4. Theoretical prediction (solid line) and experimental measurements (×) of the position of the critical layer on shadowgraph visualizations, versus the inverse of the Froude number $1/F = N/\Omega_0(0)$ for a Gaussian vortex. Here, $\alpha = 0.07$ rad and Re varies between 240 and 560 with a fixed Brunt–Väisälä frequency $N = 1.5\,\mathrm{rad\,s^{-1}}$.

3.2. *Theoretical formulation of the problem*

Our goal is to provide the basic flow solution for a vortex in a stratified fluid, whose axis is tilted with an angle α with respect to the gravity (i.e. the density gradients). The flow is governed by the Navier–Stokes equations together with the density equation and the incompressibility condition, which are in dimensional form:

$$\frac{\mathrm{D}\boldsymbol{u}}{\mathrm{D}t} = -\frac{1}{\rho}\nabla p - g\boldsymbol{e}_z + \nu\Delta\boldsymbol{u}, \tag{3.1a}$$

$$\frac{\mathrm{D}\boldsymbol{\rho}}{\mathrm{D}t} = \kappa\Delta\rho, \tag{3.1b}$$

$$\nabla\cdot\boldsymbol{u} = 0. \tag{3.1c}$$

As was discussed at the end of § 2.2, the non-dimensional problem is defined by the angle α, the Froude number F, the length ratio L, the Reynolds number Re and the Schmidt number Sc. In particular, note that the dimensionless form of the acceleration due to gravity g is L/F^2.

To determine the tilted vortex solution, the main idea is to use the new variables:

$$x' = x - \tan\alpha z, \quad y' = y, \quad z' = z. \tag{3.2}$$

Equations (3.1) can then be written, in cylindrical coordinates, as:

$$\frac{\mathrm{D}u}{\mathrm{D}t} - \frac{v^2}{r'} - w\tan\alpha\frac{\partial u}{\partial x'} - w\frac{\tan\alpha\sin\theta'}{r'}v = -\frac{1}{\rho}\frac{\partial p}{\partial r'} + \frac{(\Delta'\boldsymbol{u})_r}{Re}, \tag{3.3a}$$

$$\frac{\mathrm{D}v}{\mathrm{D}t} + \frac{uv}{r'} - w\tan\alpha\frac{\partial v}{\partial x'} + w\frac{\tan\alpha\sin\theta'}{r'}u = -\frac{1}{\rho r'}\frac{\partial p}{\partial\theta'} + \frac{(\Delta'\boldsymbol{u})_\theta}{Re}, \tag{3.3b}$$

$$\frac{\mathrm{D}w}{\mathrm{D}t} - w\tan\alpha\frac{\partial w}{\partial x'} = -\frac{1}{\rho}\frac{\partial p}{\partial z'} + \frac{\tan\alpha}{\rho}\frac{\partial p}{\partial x'} - \frac{L}{F^2} + \frac{\Delta' w}{Re}, \tag{3.3c}$$

$$\frac{\mathrm{D}\rho}{\mathrm{D}t} - w\tan\alpha\frac{\partial\rho}{\partial x'} = \frac{\Delta'\rho}{Re\,Sc}, \tag{3.3d}$$

$$\frac{1}{r'}\frac{\partial(r'u)}{\partial r'} + \frac{1}{r'}\frac{\partial v}{\partial\theta'} + \left(\frac{\partial}{\partial z'} - \tan\alpha\frac{\partial}{\partial x'}\right)w = 0, \tag{3.3e}$$

with

$$\frac{\mathrm{D}}{\mathrm{D}t} = \left(\frac{\partial}{\partial t} + u\frac{\partial}{\partial r'} + \frac{v}{r'}\frac{\partial}{\partial\theta'} + w\frac{\partial}{\partial z'}\right), \quad \frac{\partial}{\partial x'} = \cos\theta'\frac{\partial}{\partial r'} - \frac{\sin\theta'}{r'}\frac{\partial}{\partial\theta'}.$$

In these equations, u and v are the radial and azimuthal components of the horizontal velocity field in the polar coordinate system (r', θ') deduced from (x', y') while w is the velocity component along the direction of the gravity field (z-axis). In the following, the primes are dropped.

When the vortex is not tilted ($\alpha = 0$), we recover the classical equations for the dynamics of a vertical stratified vortex. A stationary axisymmetric solution is known to exist in the form $(u, v, w, p, \rho) = (0, r\Omega_0(r), 0, p_0(r, z), \rho_0(r, z))$ provided that

$$r\Omega_0^2 = \frac{1}{\rho_0}\frac{\partial p_0}{\partial r}, \quad -\frac{1}{\rho_0}\frac{\partial p_0}{\partial z} = \frac{L}{F^2}. \tag{3.4a, b}$$

These two equations express the cyclostrophic and the hydrostatic equilibrium with no interaction between the density field and the velocity field. If we further assume that the stratification length L is independent of z, the general solution is found, for any angular velocity profile $\Omega_0(r)$ as:

$$\rho_0 = \mathrm{e}^{-z/L}\ \exp\left(\frac{F^2}{L^2}\int^r r'\Omega_0^2(r')\,\mathrm{d}r'\right), \tag{3.5a}$$

$$p_0 = N^2L^2\,\mathrm{e}^{-z/L}\exp\left(\frac{F^2}{L^2}\int^r r'\Omega_0^2(r')\,\mathrm{d}r'\right). \tag{3.5b}$$

This solution has been obtained in the absence of the Boussinesq approximation.

We now wish to solve these equations for a finite tilt angle α.

3.3. *Expansion for small tilt angles*

For small α, inclination is expected to modify the flow field only weakly. Thus, it is natural to use a perturbation approach. Velocity, pressure and density fields are thus expanded as:

$$\boldsymbol{u} = \boldsymbol{u}_0 + \tan\alpha\boldsymbol{u}_1 + \cdots, \tag{3.6a}$$

$$p = p_0(1 + \tan\alpha p_1(F/L)^2 + \cdots), \tag{3.6b}$$

$$\rho = \rho_0(1 + \tan\alpha\rho_1/L + \cdots), \tag{3.6c}$$

where $(\boldsymbol{u}_0, p_0, \rho_0)$ is the vertical solution and $(\boldsymbol{u}_1, p_1, \rho_1)$ is the non-dimensional first-order correction due to inclination with $\alpha \ll 1$ so that $\tan\alpha \sim \alpha$.

The introduction of (3.6) into (3.3) and linearizing with respect to α yields, at leading order, a solution (u_0, p_0, ρ_0) given by (3.5), as in the vertical case. At order α, equations (3.3) become:

$$\left(\frac{\partial}{\partial t} + \Omega_0\frac{\partial}{\partial\theta}\right)u_1 - 2\Omega_0 v_1 = -\frac{\partial p_1}{\partial r} - r\Omega_0^2\left(\frac{\rho_1}{L} - \frac{p_1F^2}{L^2}\right) + \frac{(\Delta\boldsymbol{u}_1)_r}{Re}, \tag{3.7a}$$

$$\left(\frac{\partial}{\partial t} + \Omega_0\frac{\partial}{\partial\theta}\right)v_1 + \omega_0 u_1 = -\frac{1}{r}\frac{\partial p_1}{\partial\theta} + \frac{(\Delta\boldsymbol{u}_1)_\theta}{Re}, \tag{3.7b}$$

$$\left(\frac{\partial}{\partial t}+\Omega_0\frac{\partial}{\partial\theta}\right)w_1=-\frac{\partial p_1}{\partial z}-\frac{\rho_1}{F^2}+r\Omega_0^2\cos\theta+\frac{p_1}{L}+\frac{\Delta w_1}{Re}, \tag{3.7c}$$

$$\left(\frac{\partial}{\partial t}+\Omega_0\frac{\partial}{\partial\theta}\right)\rho_1=w_1-\frac{r\Omega_0^2F^2u_1}{L}+\frac{\Delta\rho_1}{Re\,Sc}, \tag{3.7d}$$

$$\frac{1}{r}\frac{\partial(ru_1)}{\partial r}+\frac{1}{r}\frac{\partial v_1}{\partial\theta}+\frac{\partial w_1}{\partial z}=0, \tag{3.7e}$$

where $\omega_0=(1/r)(\mathrm{d}(r^2\Omega_0)/\mathrm{d}r)$ is the vorticity of the vortex. Note that the only forcing term in these equations corresponds to $r\Omega_0^2\cos\theta$, which is a buoyancy force generated by the inclination of the isolevels of pressure. This term can guide us to determine the form of the solution.

To simplify the analysis, we shall now apply the Boussinesq approximation. This approximation amounts to considering the limit $L\to\infty$ in the above equations. The first-order corrections induced by non-Boussinesq effects are provided in the Appendix. Under the Boussinesq approximation, a simple inviscid and stationary solution (that is if we assume also $Re\to\infty$) can be obtained as

$$u_1=v_1=p_1=0,\quad w_1=\frac{r\Omega_0^3}{\Omega_0^2-F^{-2}}\sin\theta,\quad \rho_1=-\frac{r\Omega_0^2}{\Omega_0^2-F^{-2}}\cos\theta. \tag{3.8a, b, c}$$

This solution shows that inclination affects the axial component of the velocity and the density field only. However, it can be noted that this solution diverges at the critical point where the angular velocity $\Omega_0(r)$ is equal to the Brunt–Väisälä frequency N. This singularity can be understood as a resonance of the forcing created by the tilt of the vortex with the natural oscillating frequency of the fluid. Note also that the axial velocity in the vertical longitudinal plane (i.e. for $\theta=0$) should always be zero. This is not what has been observed in the experiments (see figure 3*b*). We shall see below that this can be explained by considering viscous effects in the neighbourhood of the critical point.

4. Critical-layer region

4.1. *Viscous critical-layer analysis*

The critical-layer singularity which is observed in the linear inviscid solution (3.8) can be smoothed by introducing additional effects such as viscosity, diffusivity or nonlinearity. For small angles, it is natural to consider viscosity as the main effect (we shall provide a more precise justification below by estimating the first nonlinear terms). The structure of the solution near the critical-point singularity is thus provided in a viscous critical layer. Viscous critical layers have been studied for many years in shear flows (see Drazin & Reid (1981) for details and references).

The idea is to introduce a new local variable $\tilde r=(r-r_c)Re^{1/3}$ on which are captured the viscous variations. The critical-layer solution is then searched in the form

$$u_1=v_1=p_1=0,\quad w_1=Re^{1/3}\tilde w_1(\tilde r)\,\mathrm{e}^{\mathrm{i}\theta}+\text{c.c.} \tag{4.1a, b}$$

$$\rho_1=Re^{1/3}\tilde\rho_1(\tilde r)\,\mathrm{e}^{\mathrm{i}\theta}+\text{c.c.}, \tag{4.1c}$$

where the condition of matching with the inviscid solution (3.8) requires that for large $\tilde r$

$$\tilde w_1\sim\frac{r_c\Omega_{0c}^2}{2i\Omega'_{0c}\tilde r},\quad \tilde\rho_1\sim-\frac{r_c\Omega_{0c}}{2\Omega'_{0c}\tilde r}. \tag{4.2a, b}$$

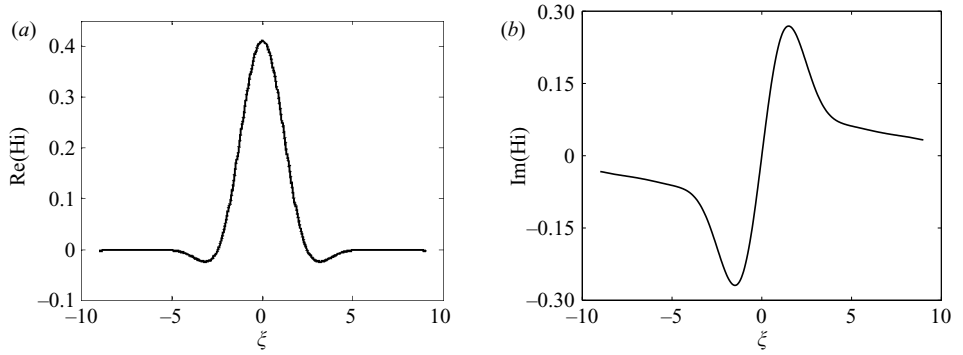

FIGURE 5. (*a*) Real part and (*b*) imaginary part of the critical-layer solution $\mathrm{Hi}(i\xi)$ versus ξ.

In the above expressions, the index c indicates values taken at r_c; Ω_{0c}' denotes the derivative of $\Omega_0(r)$ evaluated at r_c. Note that the critical-layer condition implies $\Omega_{0c} = 1/F$.

The equations for $\tilde{w}_1$ and $\tilde{\rho}_1$ are obtained by substituting (4.1) into (3.7) with $L = \infty$ and by considering the leading order in the power of $Re^{-1/3}$. This gives

$$\tilde{\rho}_1 = -\mathrm{i}\frac{\tilde{w}_1}{\Omega_{0c}}, \tag{4.3}$$

and

$$\left(1 + \frac{1}{Sc}\right)\frac{\mathrm{d}^2\tilde{w}_1}{\mathrm{d}\tilde{r}^2} - 2\mathrm{i}\Omega_{0c}'\tilde{r}\tilde{w}_1 = -r_c\Omega_{0c}^2. \tag{4.4}$$

Equation (4.4) is an inhomogeneous Airy equation. As explained in the Appendix of Drazin & Reid (1981), the solution of (4.4) which has the asymptotic behaviour (4.2*a*) is a 'balanced' generalized Airy function $B_k(K\tilde{r}, 1)$. This solution can also be expressed in terms of the Scorer's function $\mathrm{Hi}(\xi)$ (see Abramowitz & Stegun 1965, p. 448) which satisfies

$$\frac{\mathrm{d}^2\mathrm{Hi}}{\mathrm{d}\xi^2} - \xi\,\mathrm{Hi} = \frac{1}{\pi}, \tag{4.5a}$$

$$\mathrm{Hi}(\xi) \sim -\frac{1}{\pi\xi} \quad \text{as} \quad |\xi| \to \infty \quad \text{with} \quad |\arg(\xi)| > \frac{\pi}{3}. \tag{4.5b}$$

The axial velocity amplitude $\tilde{w}_1$ thus reads

$$\tilde{w}_1(\tilde{r}) = \frac{\pi r_c\Omega_{0c}^2}{|2\Omega_{0c}'|^{2/3}}\mathrm{Hi}\left(\mathrm{i}|2\Omega_{0c}'|^{1/3}\tilde{r}\right), \tag{4.6}$$

where we have implicitly assumed $Sc = \infty$. The same solution is also obtained when the diffusion of the density is taken into account by multiplying the Reynolds number by the factor $(1 + 1/Sc)^{-1}$.

Equation (4.3) tells us that the density amplitude $\tilde{\rho}_1$ exhibits the same variations as the axial velocity but with a $\pi/2$ phase shift. The Scorer function Hi with a complex argument has both a real and an imaginary part. Their variations with respect to its argument are shown in figure 5. These variations imply that contrarily to the inviscid outer solution, axial velocity and density are now expected to exhibit radial variations in all angular directions. In the vertical longitudinal plane ($\theta = 0$), the axial velocity varies as $\mathrm{Im}(\mathrm{Hi}(\mathrm{i}z))$ (figure 5*a*), while density varies as $\mathrm{Re}(\mathrm{Hi}(\mathrm{i}z))$ (figure 5*b*). In the

tilted longitudinal plane ($\theta = \pi/2$), it is the opposite. These typical variations do not depend on the vortex profile. However, the local value at the critical point r_c of the angular velocity and its radial derivative intervenes in the solution as scaling factors.

A few characteristic features of the solution in the vertical and tilted longitudinal planes can easily be provided. In the vertical longitudinal plane, the axial velocity has a jet-like profile. If we return to initial variables, the maximum velocity and the width at mid-height of the jet are given, respectively, by

$$w_{max}^{(jet)} = 0.81 \frac{r_c \Omega_{0c}^2}{|\Omega'_{0c}|^{2/3}} Re^{1/3} \tan\alpha, \tag{4.7a}$$

$$\delta^{(jet)} = \frac{2.3}{|Re\Omega'_{0c}|^{1/3}}. \tag{4.7b}$$

In the tilted longitudinal plane, the axial velocity has a shear-layer profile. The maximum absolute velocity and the distance between minimum and maximum velocities are, respectively,

$$w_{max}^{(shear)} = 0.56 \frac{r_c \Omega_{0c}^2}{|\Omega'_{0c}|^{2/3}} Re^{1/3} \tan\alpha, \tag{4.8a}$$

$$\delta^{(shear)} = \frac{2.65}{|Re\Omega'_{0c}|^{1/3}}. \tag{4.8b}$$

For instability considerations, it is also useful to compute the maximum vorticity of the jet and shear-layer profiles. They are given by

$$\omega_{max}^{(jet)} = 0.6 \frac{r_c \Omega_{0c}^2}{|\Omega'_{0c}|^{1/3}} Re^{2/3} \tan\alpha, \tag{4.9a}$$

$$\omega_{max}^{(shear)} = 0.74 \frac{r_c \Omega_{0c}^2}{|\Omega'_{0c}|^{1/3}} Re^{2/3} \tan\alpha. \tag{4.9b}$$

For large Reynolds numbers or important α, viscosity may not be the dominant effect in the critical layer. Nonlinearity may become more important. The importance of nonlinear effects in the viscous critical-layer can be estimated by introducing the viscous critical-layer solution into the governing equations (3.3) rewritten with the viscous critical-layer variable. Under the Boussinesq approximation, the radial velocity is deduced from (3.3*e*):

$$\tilde{u} = \alpha^2 Re^{1/3} \mathrm{Re}(\tilde{w}_1(\tilde{r})\, \mathrm{e}^{\mathrm{i}\theta}) + O(\alpha^2). \tag{4.10}$$

This expression permits us to show that the dominant convective term $\alpha w \partial_x$ simplifies with $u\partial_r$ such that the nonlinear terms in the (3.3*c*) for w are only $O(\alpha^3 Re^{2/3})$. These terms have to be compared to the viscous term $\Delta w/Re$ which is $O(\alpha)$. They are therefore negligible as long as $\alpha Re^{1/3} \ll 1$. In view of (4.7), this condition is equivalent to assuming that the amplitude of the axial velocity correction remains small. This condition is therefore not restrictive, as a fully nonlinear regime is expected for $O(1)$ amplitudes. It is worth mentioning that a different conclusion is reached in classical critical-layer studies (see for instance Maslowe 1986) where a nonlinear regime is obtained for small amplitudes of order $Re^{-2/3}$.

4.2. *Experimental measurements*

In this section, experimental measurements are compared to the theoretical profiles predicted by the viscous critical-layer analysis performed in the previous section.

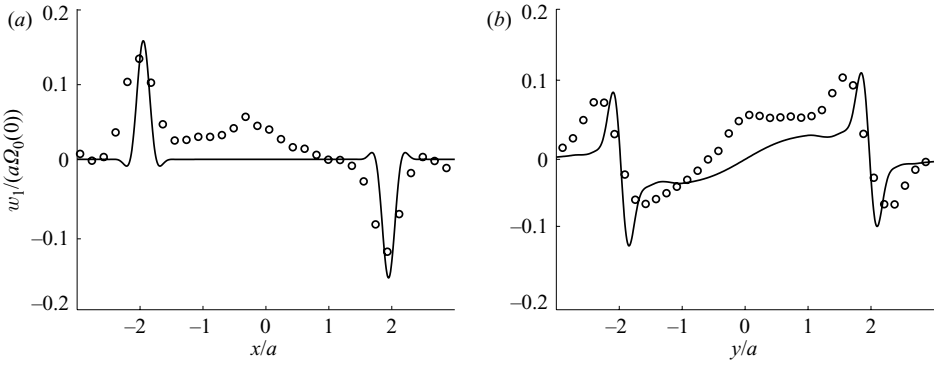

FIGURE 6. Theoretical (solid line) and experimental (circles) axial velocity profiles in two different longitudinal planes, (*a*) $\theta = 0$, (*b*) $\theta = \pi/2$. $Re = 560$, $F = 4.3$ and $\alpha = 0.07$ rad.

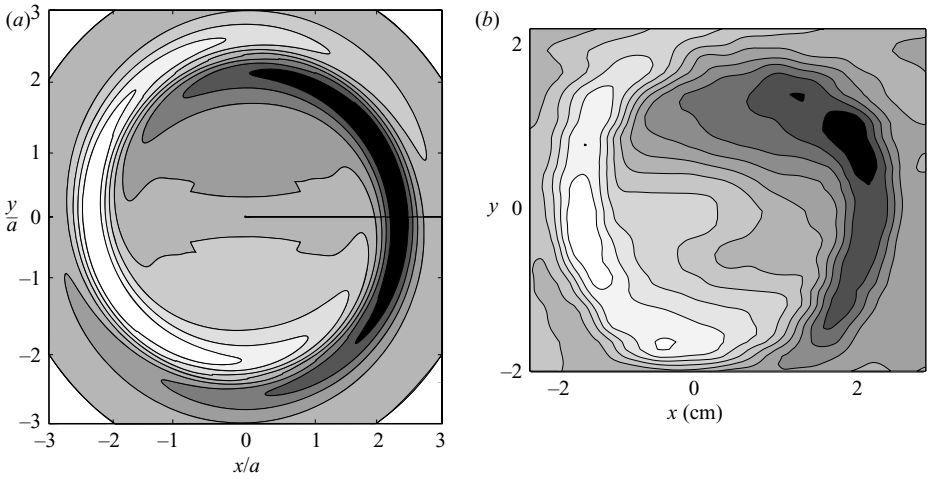

FIGURE 7. (*a*) Theoretical and (*b*) experimental axial velocity contours in a plane perpendicular to the vortex axis. $Re = 450$, $F = 3.2$ and $\alpha = 0.07$ rad.

As explained in § 2.1, visualizations and PIV measurements are made in two perpendicular longitudinal planes corresponding to the $\theta = 0$ and $\theta = \pi/2$ directions. Figure 6 shows the axial velocity profiles measured in these two planes. These profiles have been obtained by averaging the PIV measurements along the vortex axis. They are compared to theoretical profiles obtained from the critical-layer analysis for the experimental parameters. Both the jet and shear-layer profiles are observed in the critical-layer region in the $\theta = 0$ and $\theta = \pi/2$ planes, respectively, in qualitative agreement with the theory. The theory slightly underestimates the largest velocities, but it provides a good estimate of the widths of the jet and of the shear layer. However, note that between the two critical-layer regions, the experimental velocity profile is not as smooth as expected from the theory. We think that this is due to the strong diffraction of the luminous rays across the critical layer, which makes the PIV images blurred near the vortex centre and therefore less accurate. It is also worth mentioning that for the experimental data shown in figures 6 and 7, the parameter $\alpha Re^{1/3}$ which measures the strength of the nonlinear effects is not very small (it is

close to 0.5). The discrepancies in the critical layer could therefore also be due to nonlinear effects.

In figure 7, the isocontours of axial velocity in a plane perpendicular to the vortex axis are shown. The theoretical plot is obtained by using (4.1) and (4.6) for θ varying between 0 and 2π. The experimental plot has been obtained by constructing the data from measurements made in a longitudinal plane. We have used the properties that the vortex slowly moves away from the flap, so that the whole volume can be scanned by a fixed plane if this plane is placed perpendicular to the direction of displacement of the vortex. Measurements in this plane of the axial velocity have been made at a rate of 5 velocity fields per second. A total of 48 vertical velocity fields have been used to reconstruct the velocity field in figure 7(*b*). We have not been able to scan a larger volume because of lack of computer memory. Despite this limitation, the main features of the critical-layer solutions are clearly visible in the experimental measurements. Note, in particular, that the azimuthal dependency of the solution is reproduced well. This result, together with the good agreement observed for the radial profiles, validates the theoretical description in terms of the viscous critical-layer solution.

5. Conclusion

The dynamics of a vortex in a stratified fluid whose axis is slightly tilted with respect to the direction of stratification has been investigated theoretically and experimentally. For moderate Froude number $Fr \approx 1$–5 and large Reynolds numbers $Re = 240$–800, we have observed by using strioscopic visualizations and PIV measurements that strong density and axial flow variations are generated around the vortex near a particular radial location when the vortex is tilted by a few degrees. We have shown that this location corresponds to a critical point where the angular velocity of the vortex equals the Brunt–Väisälä frequency of the stratified medium.

A theoretical model has been constructed to describe these experimental observations. The critical point has been shown to correspond to a singularity of the linear inviscid correction to the vortex induced by tilting. A viscous critical-layer analysis has been performed to smooth the singularity and the critical-layer solution has been demonstrated to describe correctly the measured axial velocity profiles. The theory has also provided the main characteristics of the flow generated by tilting. In particular, we have shown that density variations can be deduced from axial velocity variations by a $\pi/2$ angular phase shift. The axial velocity variations exhibit a strong shear with a maximum vorticity of order $\alpha Re^{2/3}$ in the tilted longitudinal plane ($\theta = \pi/2$) and a jet-like structure in the vertical longitudinal plane ($\theta = 0$).

Note also that when the Froude number is smaller than 1, that is, the Brunt–Väisälä frequency is larger than any angular velocity of the vortex, there is no critical-point singularity and the linear inviscid solution (3.8) is expected to provide a description, at least for small angles, of the correction induced by tilting at any point.

It is important to remember that we have focused on small inclination angles and large Reynolds numbers. For large inclination angles, nonlinear effects should become important. For Froude numbers larger than 1, these effects are expected to appear first near the critical point where the correction amplitude is the largest. As explained above, the nonlinear transition should occur when $\alpha Re^{1/3}$ becomes large, that is when axial velocity corrections become $O(1)$.

The stability of the tilted stratified vortex solution we have obtained has not been addressed in this paper. Experimental observations do demonstrate that a

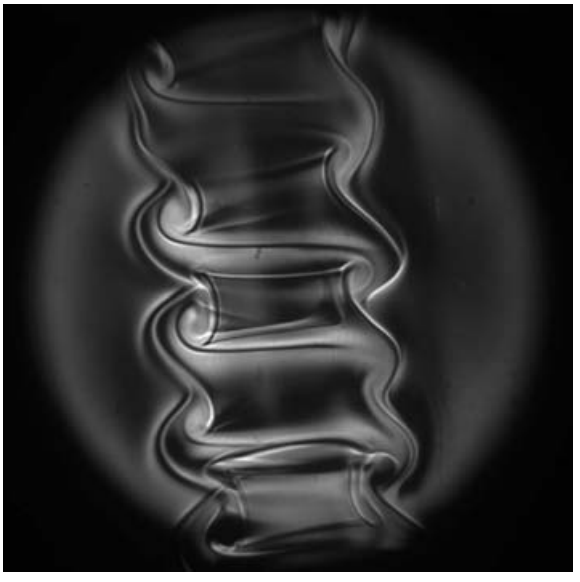

FIGURE 8. Instability of a stratified tilted vortex. Strioscopic visualization of the configuration shown in figure 3(*a*), 3.5 rotation periods later.

three-dimensional instability is indeed active under certain conditions. Figure 8 is a typical visualization by strioscopy of the density variations when instability is present. Coherent co-rotating vortical structures apparently develop in the critical-layer region. The characteristics of the critical-layer solution allow at least two possible instability mechanisms: the strong shear generated in the critical layer could be responsible for a Kelvin–Helmholtz-like instability whereas density variations coupled with the centrifugal force could be the source of a Rayleigh–Taylor instability. The comprehensive analysis of this instability is the subject of a companion paper (Boulanger *et al.* 2007).

We would like to stress that both the generation of the strong axial shear and density variation and its further destabilization occur for very small inclination angles. For this reason, we believe that this phenomenon is a generic feature affecting any intense vortex in a stratified fluid, provided its Froude number is larger than 1. The experiments performed by Cariteau (2005) have confirmed this point, as the same phenomenology has been observed although the vortex was not supposed to be tilted.

Appendix. Non-Boussinesq corrections

In this section, we provide the first-order correction to the tilted vortex solution induced by non-Boussinesq effects.

Outside the critical layer, the density and axial velocity perturbations are provided at leading order by (3.8*c*). These variations induced small perturbations of order $1/L$ for the radial and azimuthal velocity and the pressure. If we expand these components as

$$u_1 = \frac{u_1^{(1)} \sin\theta}{L} + O\left(\frac{1}{L^2}\right), \quad v_1 = \frac{v_1^{(1)} \cos\theta}{L} + O\left(\frac{1}{L^2}\right), \tag{A 1a, b}$$

$$p_1 = \frac{p_1^{(1)} \cos\theta}{L} + O\left(\frac{1}{L^2}\right), \tag{A 1c}$$

we obtain the following equations for $u_1^{(1)}$, $v_1^{(1)}$ and $p_1^{(1)}$:

$$\Omega_0 u_1^{(1)} - 2\Omega_0 v_1^{(1)} = -\frac{\mathrm{d}p_1^{(1)}}{\mathrm{d}r} + \frac{r^2\Omega_0^4}{\Omega_0^2 - F^{-2}}, \quad \Omega_0 v_1^{(1)} - \omega_0 u_1^{(1)} = -\frac{p_1^{(1)}}{r}, \tag{A 2a, b}$$

$$\frac{\mathrm{d}ru_1^{(1)}}{\mathrm{d}r} = v_1^{(1)}. \tag{A 2c}$$

This system can be reduced to a single equation for $u_1^{(1)}$:

$$\frac{\mathrm{d}^2u_1^{(1)}}{\mathrm{d}r^2} + \frac{3}{r}\frac{\mathrm{d}u_1^{(1)}}{\mathrm{d}r} - \left(\frac{3\Omega_0'}{r\Omega_0} + \frac{\Omega_0''}{\Omega_0}\right)u_1^{(1)} = -\frac{\Omega_0^3}{\Omega_0^2 - F^{-2}}. \tag{A 3}$$

Since $\Omega_0(r)$ is the solution to the homogeneous part of this equation, a general solution can be obtained by the variation of the constant as

$$u_1^{(1)} = -\Omega_0(r)\int_{c_1}^{r} \frac{1}{\Omega_0^2(x)x^3}\int_{c_2}^{x} \frac{\Omega_0^4(y)y^3}{\Omega_0^2(y) - F^{-2}}\,\mathrm{d}y\,\mathrm{d}x, \tag{A 4}$$

where c_1 and c_2 are constants. These constants may be different in the regions $(0, r_c)$ and $(r_c, +\infty)$. From the boundary conditions, we find that $c_1 = c_2 = 0$ in $(0, r_c)$ and $c_2 = +\infty$ in $(r_c, +\infty)$. The latter constant can be derived from a condition of matching with the critical-layer solution. The components $v_1^{(1)}$ and $p_1^{(1)}$ can be obtained using (A 2*b*, *c*) and similar arguments.

In the critical layer, pressure corrections and radial and azimuthal velocity corrections are also created by non-Boussinesq effects. These corrections can be calculated from (3.7) using the viscous radial variable $\tilde{r} = (r - r_c)Re^{1/3}$ and keeping first-order non-Boussinesq terms only. We find that the complex amplitude of pressure and radial and azimuthal velocities expand as

$$u_1 = \frac{\tilde{u}_1^{(1)}(\tilde{r})}{LRe^{1/3}}\,\mathrm{e}^{\mathrm{i}\theta} + O\left(\frac{1}{L^2}\right), \quad v_1 = \frac{\tilde{v}_1^{(1)}(\tilde{r})}{L}\mathrm{e}^{\mathrm{i}\theta} + O\left(\frac{1}{L^2}\right), \tag{A 5a, b}$$

$$p_1 = \frac{\tilde{p}_1^{(1)}(\tilde{r})}{L}\,\mathrm{e}^{\mathrm{i}\theta} + O\left(\frac{1}{L^2}\right), \tag{A 5c}$$

and satisfy the relations

$$\frac{\mathrm{d}\tilde{p}_1^{(1)}}{\mathrm{d}\tilde{r}} = -r_c\Omega_{0c}^2\tilde{\rho}_1, \quad \tilde{v}_1^{(1)} = -\frac{\tilde{p}_1^{(1)}}{r_c\Omega_{0c}}, \quad \frac{\mathrm{d}\tilde{u}_1^{(1)}}{\mathrm{d}\tilde{r}} = -i\frac{\tilde{v}_1^{(1)}}{r_c}, \tag{A 6a, b, c}$$

where $\tilde{\rho}_1$ is given by (4.3) and (4.6). Note that the non-Boussinesq corrections of order α may be smaller than Boussinesq corrections of order α^2. For instance, the radial velocity correction given by (4.10) is larger than the correction induced by non-Boussinesq effects as soon as $\alpha Re^{2/3}L$ is large.

REFERENCES

Abramowitz, M. & Stegun, I. A. 1965 *Handbook of Mathematical Functions*. Dover.

Billant, P. & Chomaz, J.-M. 2000 Experimental evidence for a new instability of a vertical columnar vortex pair in a strongly stratified fluid. *J. Fluid Mech.* **418**, 167–188.

Booker, J. R. & Bretherton, F. P. 1967 The critical layer for internal gravity waves in a shear flow. *J. Fluid Mech.* **27**, 513–539.

Boulanger, N., Meunier, P. & Le Dizès, S. 2007 Tilt-induced instability of a stratified vortex. *J. Fluid Mech.* (submitted).

Cariteau, B. 2005 Etude de la stabilité et de l'interaction de cyclones intenses en fluide stratifié. PhD thesis, Université Joseph Fourier, Grenoble.

Cariteau, B. & Flór, J.-B. 2003 Instability of a columnar vortex in stratified fluid. *Bull. Am. Phys. Soc.* **48** (10), 164.

Drazin, P. G. & Reid, W. H. 1981 *Hydrodynamic Stability*. Cambridge University Press.

Farmer, D., Pawlowicz, R. & Jiang, R. 2002 Tilting separation flows: a mechanism for intense vertical mixing in the coastal ocean. *Dyn. Atmos. Oceans* **36**, 43–58.

Garnier, E., Métais, O. & Lesieur, M. 1996 Instabilités primaire et secondaire d'un jet barocline. *C. R. Acad. Sci. Paris* B 323, 161–168.

Hopfinger, E. J. & van Heijst, G. J. F. 1993 Vortices in rotating fluids. *Annu. Rev. Fluid Mech.* **25**, 241–289.

Kerswell, R. R. 2002 Elliptical instability. *Annu. Rev. Fluid Mech.* **34**, 83–113.

Le Dizès, S. 2000 Non-axisymmetric vortices in two-dimensional flows. *J. Fluid Mech.* **406**, 175–198.

Lesieur, M., Métais, O. & Garnier, E. 2000 Baroclinic instability and severe storms. *J. Turb.* **1**, 1–17.

Leweke, T. & Williamson, C. H. K. 1998 Cooperative elliptic instability of a vortex pair. *J. Fluid Mech.* **360**, 85–119.

Maslowe, S. A. 1986 Critical layers in shear flows. *Annu. Rev. Fluid Mech.* **18**, 405–432.

Meunier, P. & Leweke, T. 2003 Analysis and optimization of the error caused by high velocity gradients in particle image velocimetry. *Exps. Fluids* **35**, 408–421.

Meunier, P. & Leweke, T. 2005 Elliptic instability of a co-rotating vortex pair. *J. Fluid Mech.* **533**, 125–159.

Neiman, P. J., Shapiro, M. A. & Fedor, L. S. 1993 The life cycle of an extratropical marine cyclone. Part ii: mesoscale structure and diagnostics. *Mon. Weather Rev.* **121**, 2177–2199.

Pawlak, G. MacCready, P., Edwards, K. A. & McCabe, R. 2003 Observations on the evolution of tidal vorticity at a stratified deep water headland. *Geophys. Res. Lett.* **30**, 2234.

Polavarapu, S. M. & Peltier, W. R. 1993 Formation of small-scale cyclones in numerical simulations of synoptic-scale baroclinic wave life cycles: secondary instability at the cusp. *J. Atmos. Sci.* **50**, 1047–1057.